Thermodynamics and Kinetics of Refractory Multi-Principal Element Alloys: An Experimental and Modeling Comparison

R. Puerling[1], A. Miklas[1], F.G. Coury[1,2], N.R. Philips[3], P. Mason[4], N.E. Peterson[1*], A. Deal[5], J. Klemm-Toole[1], A.J. Clarke[1]

[1]Colorado School of Mines, Golden, CO 80401
[2]Universidade Federal de São Carlos, São Carlos – SP, 13565-905, Brazil
[3]Allegheny Technologies Incorporated, Albany, OR 97321
[4]Thermo-Calc Software, McMurray, PA 15317
[5]Kansas City National Security Campus, Kansas City, MO 64147

*nepeterson@mines.edu

Abstract

The search for structural alloys capable of ultrahigh temperature performance has led to the exploration of refractory multi-principal element alloys (RMPEAs). In this work, experimental results for solidification segregation and homogenization of two RMPEAs, NbTaTiW and MoNbTaTi, are compared to simulations using the Scheil and DICTRA modules in Thermo-Calc®. Scheil calculations accurately predict the observed solidification segregation, while DICTRA predicts general trends and can provide a minimum time to achieve homogenization at a given temperature.

Main

As technological advances reach their limits with currently available materials, advanced structural metallic alloys need to be discovered and developed for multiple key areas, including ultrahigh temperature performance in extreme environments. High-entropy alloys (HEAs), also referred to as multi-principal element alloys (MPEAs) or complex concentrated alloys (CCAs), have become a popular area of research during the last 15 years because they offer potential property combinations otherwise unattainable with conventional alloys. [1] The need for metallic structural alloys for use in ultrahigh temperature applications has led to the exploration of MPEAs comprised of only, or primarily, refractory metals. These alloys are known as refractory multi-principal element alloys (RMPEAs).

Although RMPEAs are capable of maintaining high strengths at elevated temperatures, their fabrication is generally limited by room and low temperature ductility, especially in the as-cast condition, making thermomechanical processing challenging. [1–10] The use of thermodynamic simulation programs, such as Thermo-Calc®, has been demonstrated as useful tools for screening of potential compositions in alloy design studies in a wide variety of alloy systems, including steels [11–13], aluminum [14,15], Ni-based alloys [16], and MPEAs [4,17,18]. This work compares experimental data with predictions of the solidification and homogenization behavior of the equimolar RMPEAs NbTaTiW and MoNbTaTi using Thermo-Calc®.

The Scheil-Gulliver model [19,20] and DICTRA module [21] available in Thermo-Calc® (Version 2021a) were used to simulate spatial variations in composition during solidification and homogenization, respectively, of the NbTaTiW and MoNbTaTi alloys. For the simulations, the TCHEA4 and MOBHEA2 databases were used to provide the thermodynamic and mobility data, respectively. The initial segregation results obtained from Scheil-Gulliver simulations were subsequently used to initialize the homogenization simulations. To explore the effects of the solidification microstructure on the homogenization kinetics, homogenization simulations were run with effective secondary dendrite arm spacings of 1000, 100, and 10 µm. The parameter used in Thermo-Calc® to capture secondary dendrite arm spacing is length scale. These were chosen to see the difference the order of magnitude makes on the simulations. Length scale is the distance over which segregation can be observed and is representative of the distance from the center of a secondary dendrite arm to the center of the interdendritic region adjacent to it and is therefore proportional to the secondary dendrite arm spacing. The simulated homogenization treatment was 35 hours at 1673K.

The measured compositions of the NbTaTiW and MoNbTaTi alloys investigated in this work are shown in Table 1. The alloys listed in Table 1 were produced by Allegheny Technologies Incorporated, in collaboration with the Center for Advanced Non-Ferrous Structural Alloys at the Colorado School of Mines. Additional details regarding sample preparation are provided in [8,10]. These alloys were made by non-consumable arc melting of high quality, remelt grade elements in an inert argon atmosphere. Each button was re-melted three times to achieve a well-mixed sample.

Table 1: Bulk compositions (at %) for the RMPEAs NbTaTiW and MoNbTaTi measured by EDS.

	Mo/W	**Nb**	**Ta**	**Ti**
MoNbTaTi	25.3	24.6	24.8	25.3
NbTaTiW	26.4	24.5	24.5	24.6

The alloy buttons were then heat treated under vacuum at 1673K for 35 h in an attempt to achieve homogenization. Samples in both the as-cast and heat-treated condition were ground to a 1200 grit surface finish with different SiC metallographic papers, followed by polishing with 6 µm, 3 µm, and 1 µm diamond media for about 5 min each. A final polishing step of 0.05 µm colloidal silica was performed for a total of 8 h in a vibratory polisher. The samples were then imaged and characterized using Scanning Electron Microscopy (SEM) using an FEI Quanta 600i Environmental SEM equipped with an Energy Dispersive X-Ray Spectroscopy (EDS) detector (EDAX Element). For the compositional measurements using EDS, the count time per pixel was set to 100 s and the accelerating voltage was set to 25 kV. [22] The raw counts obtained for each EDS spectra were subsequently converted to atomic fractions using the vendor supplied ZAF correction scheme (EDAX Team software).

The solidification segregation behavior prior to homogenization heat treatment has been evaluated experimentally for similar alloys. Samples of NbTaV-(Ti, W) and MoNbTaV were made by arc melting commercially pure elemental powder, each button being re-melted three times. The NbTaV-(Ti, W) samples were observed to have Ta and W-rich dendrite cores and Nb, Ti, and V-rich interdendritic regions. [23] In the MoNbTaV sample, the dendrite cores were observed to be Ta-rich, while the interdendritic regions were found to be Nb, Mo, and V-rich. [24] Therefore, in the MoNbTaTi, it is expected that the dendrite cores will be Ta-rich and the interdendritic regions will be Mo, Nb, and Ti-rich, while in the NbTaTiW, it is expected that the dendrite cores will be Ta and W-rich, and the interdendritic regions will be Nb and Ti-rich.

Back-scattered electron (BSE) micrographs of the as-cast and heat-treated (35 hours at 1673K) of the NbTaTiW alloy are shown in Figure 1. The dendritic structure in the as-cast condition, shown in Figure 1(a) indicates a secondary dendrite arm spacing of 10-30 µm. Secondary dendrite arm spacing was evaluated by taking 20 measurements from the center of different secondary dendrite arms to the center of their adjacent interdendritic regions. SEM BSE micrographs after homogenization at 1673K for 35 h also reveal contrast associated with residual compositional segregation, as shown in Figure 1(b). Figure 2 also shows similar residual compositional segregation from solidification in MoNbTaTi after homogenization at 1673K for 35 h.

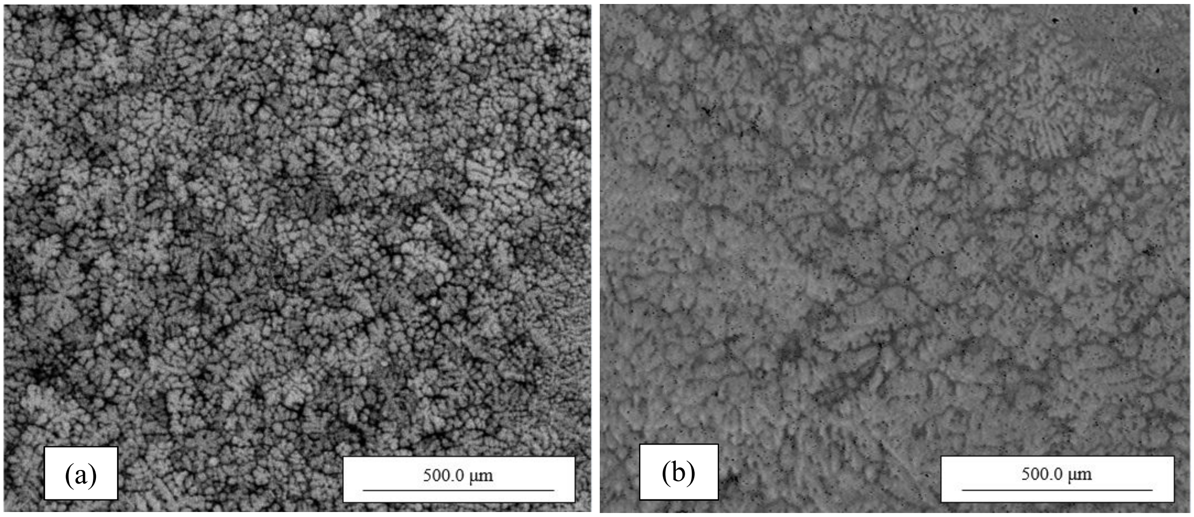

Figure 1: SEM BSE micrographs of (a) as-cast and (b) heat treated (1673K for 35 h) NbTaTiW.

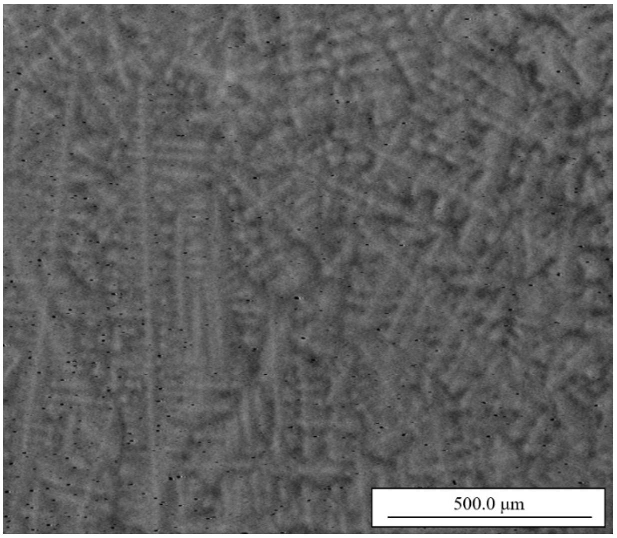

Figure 2: SEM BSE micrograph of MoNbTaTi after heat treatment at 1673K for 35 h.

The results of simulations to predict segregation from solidification and subsequent homogenization during a 1673K heat treatment for 35 h for NbTaTiW are shown in Figure 3. Figures 3(a), 3(b), and 3(c) simulate homogenization for a range of secondary dendrite arm spacings, with the 10 μm characteristic length scale resulting in almost complete removal of segregation. Similar behavior is shown in Figures 4(a), 4(b), and 4(c) for MoNbTaTi. The rate of homogenization is highly dependent on the length scale over which the solidification segregation is observed. It can be seen that the as-cast condition for both alloys mostly follow the trends predicted above; the dendrite cores are Mo, Ta, and W-rich, while the interdendritic regions are Nb and Ti-rich.

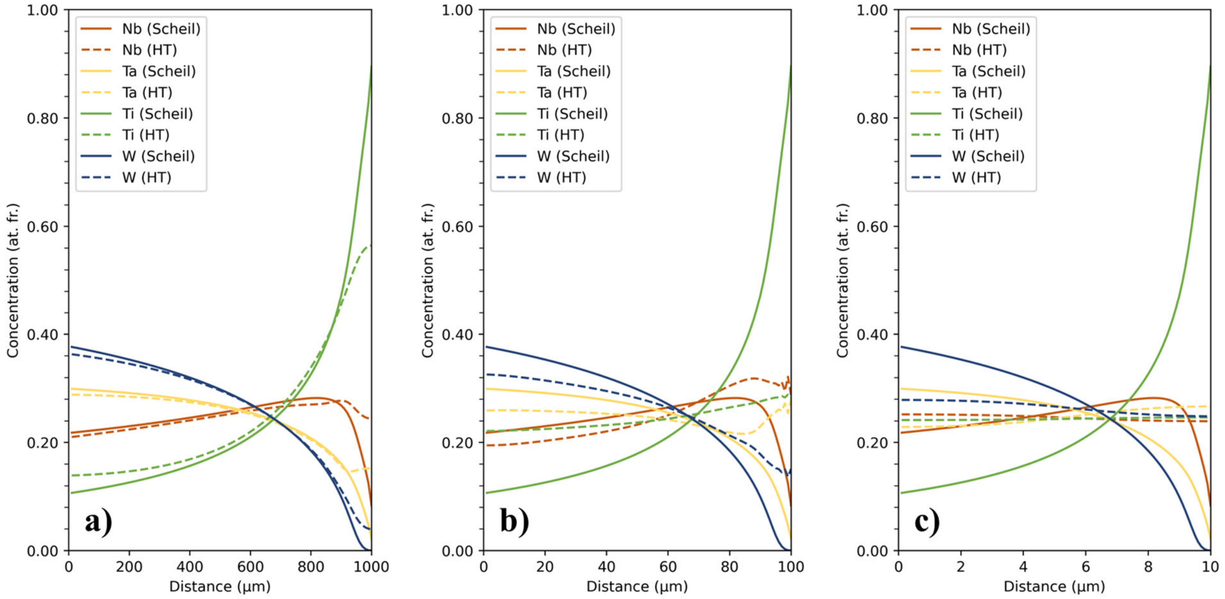

Figure 3: Solidification and homogenization simulations (35 h, 1673K) of NbTaTiW for length scales of (a) 1000 μm, (b) 100 μm, and (c) 10 μm, where Scheil is the composition profile from the Scheil calculation, HT is the composition profile from the simulated homogenization heat treatment. The distance (x-axis) is measured from the center of the secondary dendrite arm to the interdendritic region.

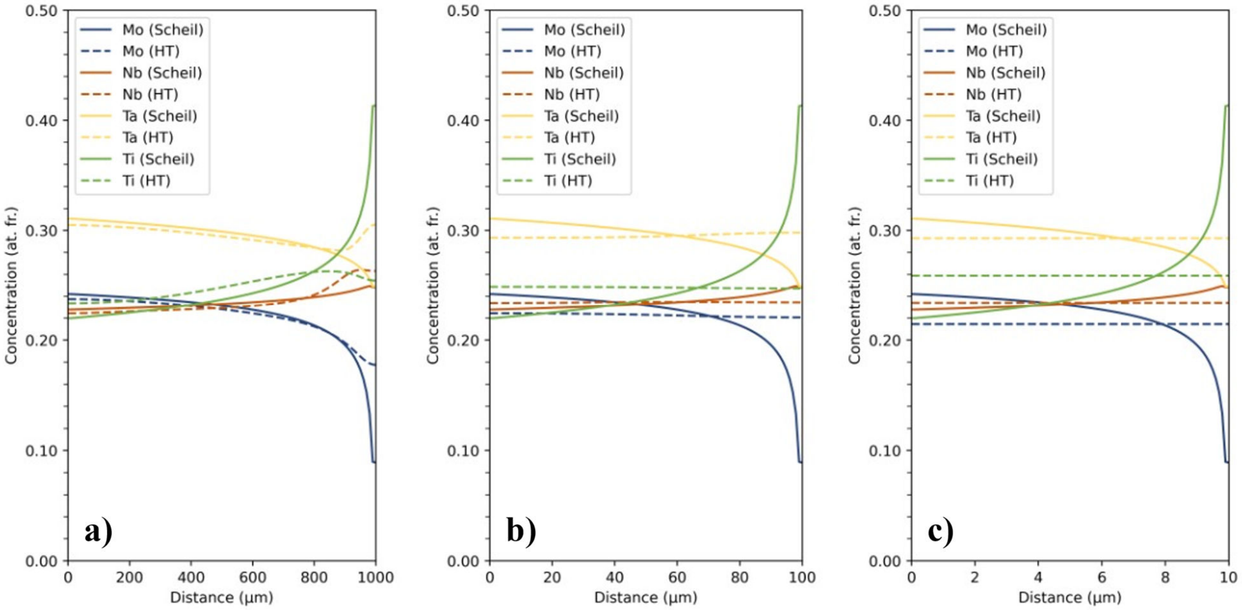

Figure 4: Solidification and homogenization simulations (35 h, 1673K) of MoNbTaTi for length scales of (a) 1000 µm, (b) 100 µm, and (c) 10 µm, where Scheil is the composition profile from the Scheil calculation, HT is the composition profile from the simulated homogenization heat treatment. The distance (x-axis) is measured from the center of the secondary dendrite arm to the interdendritic region.

Experimental EDS measurements of the principal elements at the dendrite core and interdendritic regions taken in the as-cast condition are compared to the solidification simulation results in Tables 2 and 3. The simulation results captured in Table 2 are representative of the extremes, where the dendrite core composition is taken at a distance of zero and the interdendritic composition is taken at the maximum distance from the center of the dendrite. While Nb concentration in the dendrite core is similar in both the experimental and simulation data with a difference of only 0.6 at%, all other elements have compositional differences ranging from 5.4 at% (Ta in the dendrite core) to 37.2 at% (Ti in the interdendritic region). This can be attributed to the error inherent in experimentally estimating the center of the dendrite core and interdendritic regions. If the measurements are instead assumed to be taken off-center, the solidification segregation simulation is in much better agreement, as shown in Table 3. These off-center measurements were assumed to be taken at 50% and 90% of the length-scale for the dendrite core and interdendritic regions, respectively. These locations were picked for two reasons: it is more difficult to measure the center of the dendrite core than the interdendritic region, and the composition within the dendrite core changes more gradually than the interdendritic region. Tables 4 and 5 show simulation results for dendrite cores and interdendritic regions at the various length scales and experimental EDS measurements after homogenization. Both tables include the assumption that the experimental measurements were not taken at the exact centers of the dendrite core and interdendritic region. The 1000 µm length scale simulation data agrees the most with the experimental data for both RMPEAs, although this length scale is approximately two orders of magnitude greater than measured in Figures 1 and 2. For NbTaTiW, the 100 µm simulation data remains close to the experimental data; the biggest discrepancy is observed for Ti, for which the simulation predicts it to be approximately 4 at% higher in the dendrite core than the experimental data exhibits. The 10 µm simulation is the least accurate of the length scales, as it predicts almost full homogenization after heat treatment, while Figure 1(b) shows that segregation is still present. All but the concentration of Nb in the dendrite core are off by about 2 at% or more. For MoNbTaTi, the 100 µm simulation predicts almost full homogenization, with the simulation prediction for Ta at the dendrite core differing from the experimental data by approximately 3 at%. The 10 µm simulation displays the greatest deviation from the experimental data, predicting complete homogenization, while Figure 2 shows that segregation remains after heat treatment. While the sluggish diffusion effect was considered to be a possible contributing factor in the discrepancy between the experimental results and the simulations, recent studies suggest sluggish diffusion is caused by specific compositions and is not a general HEA effect. [25,26]. It is more likely that DICTRA, with the mobility data in the MOBHEA2 database predicts faster diffusion than the actual rate observed experimentally. The simulation was successful, however, in predicting the segregation trends during solidification and heat treatment.

Table 2: As cast compositional (at%) data for experimental and simulation solidification of NbTaTiW, with simulated data taken from the extremes.

		Nb	**Ta**	**Ti**	**W**
Dendrite Core	**Experimental**	22.3	24.5	26.0	27.2
	Simulated	21.7	29.9	10.6	37.8
Interdendritic	**Experimental**	24.3	14.1	52.3	9.1
	Simulated	8.3	2.2	89.5	0.004

Table 3: As cast compositional (at%) data for experimental and simulation solidification of NbTaTiW, including the assumption experimental measurements were taken at 50% and 90% of the length-scale for the dendrite core and interdendritic region, respectively instead of the exact center of the dendrite core and interdendritic region.

		Nb	**Ta**	**Ti**	**W**
Dendrite “Core”	**Experimental**	22.3	24.5	26.0	27.2
	Simulated	27.0	24.5	23.3	25.2
Interdendritic	**Experimental**	24.3	14.1	52.3	9.1
	Simulated	25.5	14.6	52.5	7.3

Table 4: Heat treated compositional (at%) data for experiments and simulations for NbTaTiW.

			Nb	**Ta**	**Ti**	**W**
Dendrite Core	**Experimental**		23.2	27.9	19.8	29.1
	Simulated	**1000 µm**	25.1	26.4	19.3	29.2
		100 µm	23.5	24.8	23.8	27.9
		10 µm	24.6	24.5	24.3	26.6
Interdendritic	**Experimental**		26.5	23.9	26.3	23.5
	Simulated	**1000 µm**	26.6	23.4	26.5	23.6
		100 µm	28.1	22.8	25.5	23.6
		10 µm	24.2	25.8	24.5	25.5

Table 5: Heat treated compositional (at %) data for experiments and simulations for MoNbTaTi.

			Mo	**Nb**	**Ta**	**Ti**
Dendrite Core	**Experimental**		21.7	22.3	33.5	21.4
	Simulated	**1000 µm**	23.7	22.4	30.5	23.4
		100 µm	22.4	23.4	29.3	24.9
		10 µm	21.4	23.4	29.3	25.9
Interdendritic	**Experimental**		22.8	24.5	25.5	28.4
	Simulated	**1000 µm**	17.7	26.3	30.5	25.4
		100 µm	22.0	23.4	29.8	24.7

		10 µm	21.4	23.4	29.3	25.9

This discrepancy between the experimental and simulation results for homogenization of MoNbTaTi prompted additional exploration of diffusion behavior in refractory binary systems. Homogenization simulations were performed using DICTRA for the Mo/Nb, Nb/W, Ta/W, and Ti/W binary systems, for a heat treatment at 1400˚C for 35 hours. The calculated compositional profiles from these simulations are shown in Figure 5 below. As a comparison, characteristic self-diffusion lengths for Mo, Nb, Ta, Ti and W and inter-diffusion lengths for Ta in $Ta_{30}W_{70}$ and W in $Ta_{30}W_{70}$ were calculated using Equation 1, shown below, with literature values for the self-diffusion and inter-diffusion coefficients as a function of temperature, [27,28]

$$L_{\mathrm{D}} = \sqrt{D_{\mathrm{o}} e^{\left(\frac{-E}{RT}\right)} t} \qquad \text{Equation 1}$$

where L_{D} is the diffusion length, D_{o} is the diffusion coefficient, E is the activation energy for diffusion, R is the ideal gas constant, T is temperature, and t is time. Comparing the results from these two calculation methods, a discrepancy specific to the diffusivity of Ta was found.

Table 6: Calculated self-diffusion and inter-diffusion lengths (L_{D}) for a heat treatment for 35 hours at 1673K. The diffusion coefficient pre-factor, activation energies and relevant temperature ranges for both values used to calculate the diffusion lengths are also listed.

	D_0 (10^{-4} m^2s^{-1})	**E (kJ mol^{-1})**	**Applicable Temp Range (K)**	**L_{D} (µm)**
Mo (max)	8.0 [a]	488.2 [a]	1087-2500 [a]	0.24
Mo (min)	1.39 [b]	549.3 [b]	1363-2724 [b]	0.111
Nb (max)	1.1 [a]	401.9 [a]	1224-2668 [a]	2.0
Nb (min)	3.7 [a]	438.0 [a]	1354-2692 [a]	0.99
Ta (max)	0.124 [a]	413.2 [a]	1523-2576 [a]	0.443
Ta (min)	0.21 [a]	423.6 [a]	1261-2993 [a]	0.40
Ti (max)	4.54×10^{-4} [a]	131.0 [a]	1228-1784 [a]	682
Ti (min)	1.09 [a]	251.2 [a]	1172-1813 [a]	444
W (max)	0.04 [a]	525.8 [a]	1705-3409 [a]	0.004
W (min)	46 [a]	665.7 [a]	1705-3409 [a]	0.00098

Ta in Ta$_{30}$W$_{70}$	1.8 ^{b}	553.9 ^{b}	1573-2373 ^{b}	0.011
W in Ta$_{30}$W$_{70}$	0.17 ^{b}	510.8 ^{b}	1573-2373 ^{b}	0.016

^{a}Ref. [27], ^{b}Ref. [28]

The simulation (Figure 5(c)) predicts the TaW diffusion couple diffuses about 100 μm (measured at 25 at%), while the calculated characteristic diffusion length only predicts diffusion of less than 0.1 μm. It is recognized that the interdiffusion coefficient for the relevant binary system, which depends upon composition, is necessary to perform a homogenization simulation. Unfortunately, the availability of interdiffusion data is more limited than self-diffusion data, which is why only two interdiffusion calculations were performed to verify order of magnitude. Given the only interdiffusion coefficients used were that of Ta and W in Ta$_{30}$W$_{70}$, the discrepancy between the simulated TaW diffusion couple and the calculations remains.

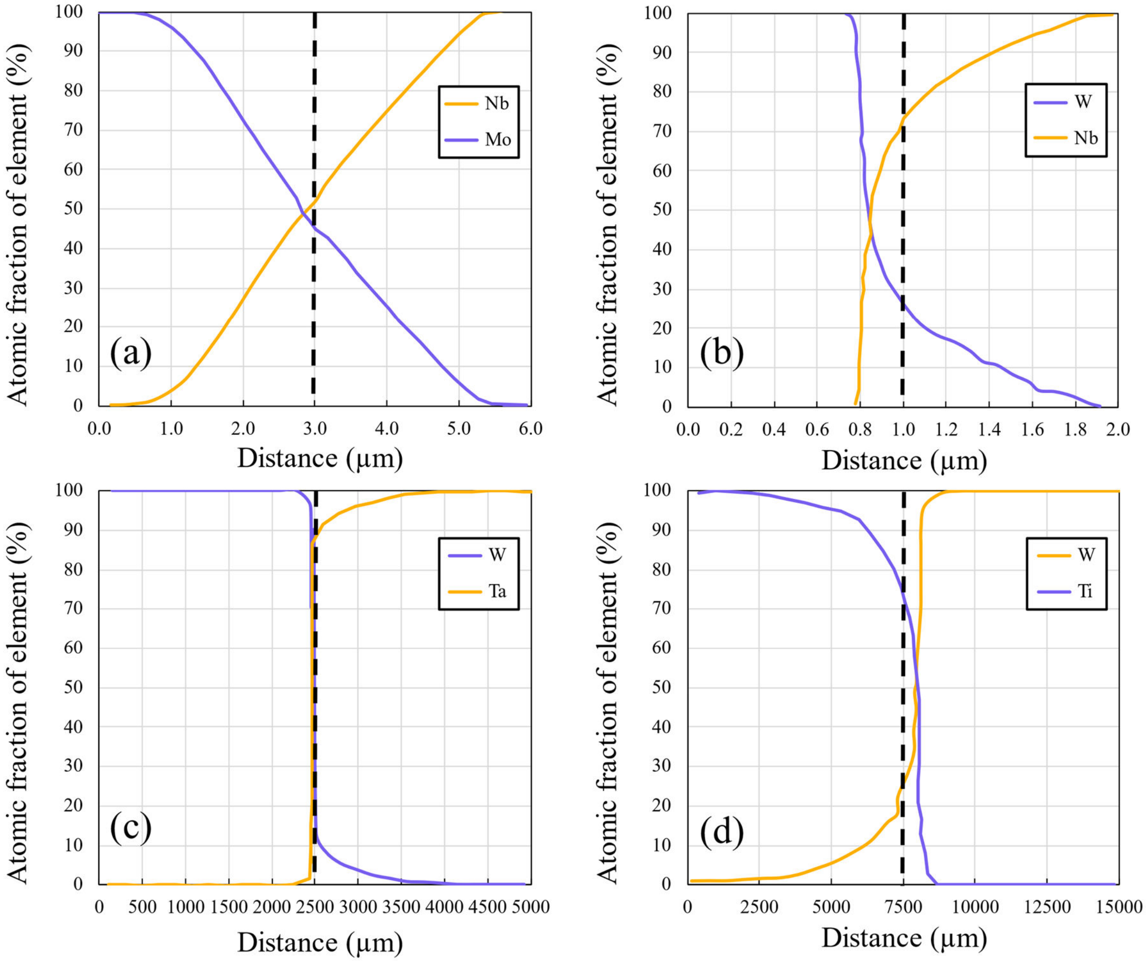

Figure 5: Diffusion couple simulations of (a) MoNb, (b) NbW, (c) TaW, and (d) TiW after a heat treatment of 35 hours at 1673K. The original interface position is shown with a black dashed line.

The predicted solidification segregation from the Scheil-Gulliver model using compared well with the experimental data. However, the homogenization simulations using DICTRA did not agree with the experimental data, predicting homogenization to occur in much shorter times than was actually observed. After analyzing the diffusion couple simulation results, it can be hypothesized that the faster than experimentally observed homogenization of the two RMPEAs studied can be attributed to the diffusivity of Ta within the MOBHEA2 database. The rest of the diffusion couple results agree with the rough diffusion calculations, suggesting DICTRA would be accurate in simulating RMPEA alloys without Ta. That said, the simulations are valuable to show qualitative trends. As the length scale of the solidification segregation decreases, the simulations predict the degree of homogeneity to increase, given a heat-treatment at 1673K for 35 h. This trend agrees with theory, when assuming the concentration of each element varies sinusoidally with distance in one dimension. The simulation is being performed over half a period, starting at either the maximum or minimum, depending on the element. The amplitude (β) of the concentration profile after a time (t) is given by the following equation:

$$\beta = \beta_0 exp \frac{-t\pi^2 D_{\mathrm{B}}}{l^2} \qquad \text{Equation 2}$$

where β_0 is the amplitude at t = 0, D_{B} is the diffusion coefficient of the element in question, and l is the length scale. [29]. This equation shows that decreasing the length scale, while keeping all else constant, will decrease the amplitude, which is exactly what the simulations predict.

In summary, due in large part to the high melting temperatures of refractory metals and the challenges associated with obtaining experimental data, opportunity exists to continually improve available thermodynamic databases, particularly for refractory alloys and RMPEAs. Research in this area is largely guided by simulations performed using computational thermodynamic and kinetic software. Therefore, the generation of both thermodynamic and kinetic data to fill in the current knowledge gaps will be essential to advancing the state of the art in refractory alloy and heat treatment design.

The need for structural metallic alloys for use in ultrahigh temperature applications has led to the exploration of RMPEAs, largely through a combination of simulation and experiments. Simulations were performed using the Scheil-Gulliver model and DICTRA in Thermo-Calc® to predict solidification segregation and homogenization in two RMPEA alloys, namely NbTaTiW and MoNbTaTi. While the Scheil-Gulliver model can accurately predict the solidification segregation of the RMPEAs, DICTRA does not predict the extent of homogenization observed experimentally when realistic length scales are used for a 35 h, 1673K heat treatment. The homogenization heat treatments performed with realistic length scales predict homogenization to occur faster than the experimental data shows. In particular, these results suggest the diffusivity of Ta in the MOBHEA2 database may be too high. Despite some discrepancies between simulation and experiment, DICTRA predicts minimum homogenization times that can be explored by heat treatment, thereby accelerating the design of future experiments to assess the thermodynamics and kinetics of RMPEAs. Future work can include comparing the RMPEA simulations with relevant binary simulations to further distinguish inconsistencies in either the database or experimental data.

Acknowledgements

This work was funded by the Department of Energy's Kansas City National Security Campus which is operated and managed by Honeywell Federal Manufacturing Technologies, LLC under contract number DE-NA0002839. The electron microscopy and the contributions of author F.G. Coury were separately supported by the Center for Advanced Non-Ferrous Structural Alloys (CANFSA), a National Science Foundation Industry/University Cooperative Research Center (I/UCRC) [Award No. 1624836] at the Colorado School of Mines and the Conselho Nacional de Desenvolvimento Científico e Tecnológico - Brasil (CNPq) [Grant No. 424645/2018-1]. We also thank ATI for producing the experimental alloys studied here.

Conflict of Interest statement

On behalf of all authors, the corresponding author states that there is no conflict of interest.

References

[1] O.N. Senkov, D.B. Miracle, K.J. Chaput, J.-P. Couzinie, Development and exploration of refractory high entropy alloys—A review, Journal of Materials Research. 33 (2018) 3092–3128. https://doi.org/10.1557/jmr.2018.153.

[2] M.-H. Tsai, J.-W. Yeh, High-Entropy Alloys: A Critical Review, Materials Research Letters. 2 (2014) 107–123. https://doi.org/10.1080/21663831.2014.912690.

[3] J. Chen, X. Zhou, W. Wang, B. Liu, Y. Lv, W. Yang, D. Xu, Y. Liu, A review on fundamental of high entropy alloys with promising high–temperature properties, Journal of Alloys and Compounds. 760 (2018) 15–30. https://doi.org/10.1016/j.jallcom.2018.05.067.

[4] O.N. Senkov, C. Zhang, A.L. Pilchak, E.J. Payton, C. Woodward, F. Zhang, CALPHAD-aided development of quaternary multi-principal element refractory alloys based on NbTiZr, Journal of Alloys and Compounds. 783 (2019) 729–742. https://doi.org/10.1016/j.jallcom.2018.12.325.

[5] S. Praveen, H.S. Kim, High-Entropy Alloys: Potential Candidates for High-Temperature Applications - An Overview, Advanced Engineering Materials. 20 (2017) 1700645. https://doi.org/10.1002/adem.201700645.

[6] J.-P. Couzinié, O.N. Senkov, D.B. Miracle, G. Dirras, Comprehensive data compilation on the mechanical properties of refractory high-entropy alloys, Data in Brief. 21 (2018) 1622–1641. https://doi.org/10.1016/j.dib.2018.10.071.

[7] A.B. Melnick, V.K. Soolshenko, Thermodynamic design of high-entropy refractory alloys, Journal of Alloys and Compounds. 694 (2017) 223–227. https://doi.org/10.1016/j.jallcom.2016.09.189.

[8] F.G. Coury, M. Kaufman, A.J. Clarke, Solid-solution strengthening in refractory high entropy alloys, Acta Materialia. 175 (2019) 66–81. https://doi.org/10.1016/j.actamat.2019.06.006.

[9] F. Maresca, W.A. Curtin, Mechanistic origin of high strength in refractory BCC high entropy alloys up to 1900K, Acta Materialia. 182 (2020) 235–249. https://doi.org/10.1016/j.actamat.2019.10.015.

[10] F.G. Coury, T. Butler, K. Chaput, A. Saville, J. Copley, J. Foltz, P. Mason, K. Clarke, M. Kaufman, A. Clarke, Phase equilibria, mechanical properties and design of quaternary refractory high entropy alloys, Materials & Design. 155 (2018) 244–256. https://doi.org/10.1016/j.matdes.2018.06.003.

[11] U.E. Klotz, C. Solenthaler, P.J. Uggowitzer, Martensitic–austenitic 9–12% Cr steels—Alloy design, microstructural stability and mechanical properties, Materials Science and Engineering: A. 476 (2008) 186–194.

[12] T. Yamashita, K. Okuda, T. Obara, Application of thermo-calc to the developments of high-performance steels, Journal of Phase Equilibria. 20 (1999) 231–237.

[13] V. Knežević, J. Balun, G. Sauthoff, G. Inden, A. Schneider, Design of martensitic/ferritic heat-resistant steels for application at 650 C with supporting thermodynamic modelling, Materials Science and Engineering: A. 477 (2008) 334–343.

[14] A.W. Zhu, B.M. Gable, G.J. Shiflet, E.A. Starke, The Intelligent Design of Age Hardenable Wrought Aluminum Alloys, Advanced Engineering Materials. 4 (2002) 839–846. https://doi.org/10.1002/1527-2648(20021105)4:11<839::AID-ADEM839>3.0.CO;2-8.

[15] H.-L. Chen, Q. Chen, A. Engström, Development and applications of the TCAL aluminum alloy database, Calphad. 62 (2018) 154–171.

[16] P.D. Jablonski, J.A. Hawk, Homogenizing advanced alloys: thermodynamic and kinetic simulations followed by experimental results, Journal of Materials Engineering and Performance. 26 (2017) 4–13.

[17] P.L. Conway, T.P.C. Klaver, J. Steggo, E. Ghassemali, High entropy alloys towards industrial applications: High-throughput screening and experimental investigation, Materials Science and Engineering: A. 830 (2022) 142297.

[18] M. Asadikiya, Y. Zhang, L. Wang, D. Apelian, Y. Zhong, Design of ternary high-entropy aluminum alloys (HEAls), Journal of Alloys and Compounds. 891 (2022) 161836.

[19] G.H. Gulliver, The quantitative effect of rapid cooling upon the constitution of binary alloys, J Inst Met. 13 (1915) 263–291.

[20] E. Scheil, Bemerkungen zur schichtkristallbildung, International Journal of Materials Research. 34 (1942) 70–72.

[21] A. Borgenstam, L. Höglund, J. Ågren, A. Engström, DICTRA, a tool for simulation of diffusional transformations in alloys, Journal of Phase Equilibria. 21 (2000) 269–280.

[22] F.G. Coury, Solid solution strengthening mechanisms in high entropy alloys, Dissertation, Colorado School of Mines, 2018. https://repository.mines.edu/handle/11124/172516.

[23] H.W. Yao, J.W. Qiao, M.C. Gao, J.A. Hawk, S.G. Ma, H.F. Zhou, Y. Zhang, NbTaV-(Ti,W) refractory high-entropy alloys: Experiments and modeling, Materials Science and Engineering: A. 674 (2016) 203–211. https://doi.org/10.1016/j.msea.2016.07.102.

[24] H. Yao, J.-W. Qiao, M. Gao, J. Hawk, S.-G. Ma, H. Zhou, MoNbTaV Medium-Entropy Alloy, Entropy. 18 (2016) 189. https://doi.org/10.3390/e18050189.

[25] J. Dąbrowa, M. Zajusz, W. Kucza, G. Cieślak, K. Berent, T. Czeppe, T. Kulik, M. Danielewski, Demystifying the sluggish diffusion effect in high entropy alloys, Journal of Alloys and Compounds. 783 (2019) 193–207. https://doi.org/10.1016/j.jallcom.2018.12.300.

[26] W. Kucza, J. Dąbrowa, G. Cieślak, K. Berent, T. Kulik, M. Danielewski, Studies of "sluggish diffusion" effect in Co-Cr-Fe-Mn-Ni, Co-Cr-Fe-Ni and Co-Fe-Mn-Ni high entropy alloys; determination of tracer diffusivities by combinatorial approach, Journal of Alloys and Compounds. 731 (2018) 920–928. https://doi.org/10.1016/j.jallcom.2017.10.108.

[27] H. Mehrer, N. Stolica, N.A. Stolwijk, 2.2.17 Actinide group metals, Landolt-Börnstein - Group III Condensed Matter. (n.d.) 64–66. https://doi.org/10.1007/10390457_26.

[28] W.F. Gale, T.C. Totemeier, Smithells metals reference book, Elsevier, 2003.

[29] D.A. Porter, K.E. Easterling, Phase transformations in metals and alloys (revised reprint), CRC press, 2009.